Nirmatrelvir treatment of SARS-CoV-2-infected mice blunts antiviral adaptive immune responses

Valeria Fumagalli[1,2] , Pietro Di Lucia[1,2], Micol Ravà[1,2], Davide Marotta[1,2], Elisa Bono[1],
Stefano Grassi[3], Lorena Donnici[4] , Rolando Cannalire[5], Irina Stefanelli[5] , Anastasia Ferraro[5],
Francesca Esposito[6] , Elena Pariani[7], Donato Inverso[1,2] , Camilla Montesano[8], Serena Delbue[9],
Stanley Perlman[10,11] , Enzo Tramontano[6] , Raffaele De Francesco[4,12] , Vincenzo Summa[5] ,
Luca G Guidotti[1,2,*] & Matteo Iannacone[1,2,13,**]

Abstract

Alongside vaccines, antiviral drugs are becoming an integral part of our response to the SARS-CoV-2 pandemic. Nirmatrelvir—an orally available inhibitor of the 3-chymotrypsin-like cysteine protease—has been shown to reduce the risk of progression to severe COVID-19. However, the impact of nirmatrelvir treatment on the development of SARS-CoV-2-specific adaptive immune responses is unknown. Here, by using mouse models of SARS-CoV-2 infection, we show that nirmatrelvir administration blunts the development of SARS-CoV-2-specific antibody and T cell responses. Accordingly, upon secondary challenge, nirmatrelvir-treated mice recruited significantly fewer memory T and B cells to the infected lungs and mediastinal lymph nodes, respectively. Together, the data highlight a potential negative impact of nirmatrelvir treatment with important implications for clinical management and might help explain the virological and/or symptomatic relapse after treatment completion reported in some individuals.

Introduction

The COVID-19 outbreak, caused by SARS-CoV-2, has resulted in more than 670 million confirmed infections causing greater than 6.8 million deaths worldwide as of February 2023 (https://coronavirus.jhu.edu/map.html). Despite effective COVID-19 vaccines have been developed at an unprecedented pace, a vast number of people are either unwilling or unable to get vaccinated. SARS-CoV-2 is a beta-coronavirus whose RNA genome encodes for two polyproteins, pp1a and pp1ab, and four structural proteins (V'kovski *et al*, 2021). The polyproteins are cleaved by the viral papain-like protease (PL^pro) and by the viral main protease (M^pro)—the latter also referred to as 3-chymotrypsin-like cysteine protease (3CL^pro)—to yield non-structural proteins that are necessary to viral replication (Pillaiyar *et al*, 2016; Jin *et al*, 2020).

Paxlovid, a combination of an orally available M^pro inhibitor termed nirmatrelvir (Owen *et al*, 2021) and ritonavir, has received an Emergency Use Authorization (EUA) from the Food and Drug Administration (FDA) for the treatment of COVID-19 on December 22, 2021. Despite its effectiveness at reducing viral titers and the risk of progressing to severe COVID-19 (Hammond *et al*, 2022; Najjar-Debbiny *et al*, 2022), the impact of nirmatrelvir treatment on the development of adaptive immunity to SARS-CoV-2 is unknown. It is also unclear why some patients experience a surprising rebound of viral load and a rapid relapse of COVID-19 symptoms shortly after the completion of an early and effective nirmatrelvir treatment (Boucau *et al*, 2022; preprint: Dai *et al*, 2022; Gupta *et al*, 2022;

1 Division of Immunology, Transplantation, and Infectious Diseases, IRCCS San Raffaele Scientific Institute, Milan, Italy
2 Vita-Salute San Raffaele University, Milan, Italy
3 Pathology Unit, IRCCS San Raffaele Scientific Institute, Milan, Italy
4 INGM - Istituto Nazionale di Genetica Molecolare "Romeo ed Erica Invernizzi", Milan, Italy
5 Department of Pharmacy, School of Medicine and Surgery, University of Naples Federico II, Naples, Italy
6 Dipartimento di Scienze della Vita e dell'Ambiente, Cittadella Universitaria di Monserrato, Cagliari, Italy
7 Department of Biomedical Sciences for Health, University of Milan, Milan, Italy
8 Department of Chemistry, La Sapienza University, Rome, Italy
9 Department of Biomedical, Surgical and Dental Sciences, University of Milan, Milan, Italy
10 Department of Microbiology and Immunology, University of Iowa, Iowa City, IA, USA
11 Department of Pediatrics, University of Iowa, Iowa City, IA, USA
12 Department of Pharmacological and Biomolecular Sciences, University of Milan, Milan, Italy
13 Experimental Imaging Center, IRCCS San Raffaele Scientific Institute, Milan, Italy
   *Corresponding author. Tel: +39 02 2643 4799; E-mail: guidotti.luca@hsr.it
   **Corresponding author. Tel: +39 348 853 3711; E-mail: iannacone.matteo@hsr.it

Ranganath *et al*, 2022; Soares *et al*, 2022; preprint: Charness *et al*, 2022a; Charness *et al*, 2022b; preprint: Wang *et al*, 2022a,b). Viral sequencing indicates that the relapse is not associated with the selection of treatment-resistant mutations, or due to infection with different SARS-CoV-2 variants (Boucau *et al*, 2022; Gupta *et al*, 2022). Whether such rebound is part of the natural history of COVID-19 or is due to an impairment in the development of adaptive immunity necessary to complete SARS-CoV-2 clearance remains to be determined.

Results and Discussion

Here, we set out to assess the impact of nirmatrelvir treatment on the development of antiviral adaptive immunity in a well-characterized mouse model of COVID-19 based on the controlled administration of aerosolized SARS-CoV-2 to K18-hACE2 transgenic mice (Fumagalli *et al*, 2021).

Nirmatrelvir was synthesized prior to its publication (Owen *et al*, 2021) via a multistep convergent approach that differed from the reported procedure (Fu *et al*, 2020; Jin *et al*, 2020; Cannalire *et al*, 2022). Details and synthesis intermediates are shown in Fig 1A and Materials and Methods. As expected, nirmatrelvir was able to inhibit the activity of the SARS-CoV-2 M^{pro} in a dose-dependent manner, as determined by a fluorescence resonance energy transfer (FRET)-based biochemical assay performed both by preincubating the protease with the compound for 30 min at 37°C (Fig 1B) or by directly adding the substrate to the reaction (Appendix Fig S1A), as described (Owen *et al*, 2021). In the two assays, the 50% inhibitory concentration (IC_{50}) of nirmatrelvir on the M^{pro} was 47 nM (Fig 1B) and 14 nM (Appendix Fig S1A), respectively. In both procedures, we used the commercially available SARS-CoV-2 M^{pro} inhibitor GC376 (Fu *et al*, 2020; Ma *et al*, 2020; Cannalire *et al*, 2022; Luan *et al*, 2022) as positive control, showing an IC_{50} of 0.14 nM (Fig 1B) and 4.8 nM (Appendix Fig S1A), respectively. Next, the antiviral activity of nirmatrelvir against SARS-CoV-2 was examined by monitoring the protection from cytopathic effect in infected HEK293T-hACE2 cells (Fig 1C) and by quantifying SARS-CoV-2 RNA in the supernatant (Appendix Fig S1B). Nirmatrelvir prevented death of HEK293T-hACE2 cells infected with the SARS-CoV-2 variants D614G, B.1.617.2 (Delta), and B.1.1.529 (Omicron BA.1) with a mean IC_{50} value of 33 ± 10 nM (Fig 1C) and prevented SARS-CoV-2 RNA release with a mean IC_{50} value of 54 ± 25 nM (Appendix Fig S1B). Finally, we evaluated the antiviral activity of nirmatrelvir in a well-characterized mouse model of COVID-19, based on the controlled administration of aerosolized SARS-CoV-2 to K18-hACE2 transgenic mice (Fumagalli *et al*, 2021). Briefly, non-anesthetized mice were placed in a nose-only inhalation tower system and exposed to a target dose of 2×10^5 tissue culture infectious dose 50 ($TCID_{50}$) of aerosolized B.1.1.529 under controlled pressure, temperature, and humidity conditions (Fig 1D). Mice were treated six times with vehicle or nirmatrelvir via oral gavage (150 mpk/mouse) starting at 4 h post-infection (p.i.) and every 12 h thereafter up until day 3 p.i. (Fig 1D). The plasma concentration of nirmatrelvir evaluated 4 h after the last administration was 1.39 ± 0.73 μM (Appendix Fig S1C). As expected, neither SARS-CoV-2 infection nor nirmatrelvir treatment affected the body weight of K18-hACE2 mice (Fig 1E). In line with previously published studies (Fumagalli *et al*, 2021; Owen

et al, 2021), whereas vehicle-treated SARS-CoV-2-infected mice showed robust viral replication in the lungs and in the nasal turbinates, nirmatrelvir-treated SARS-CoV-2-infected mice showed virtually undetectable viral RNA and infectious virus in the same anatomical compartments (Fig 1F and G).

With this established system, we next set out to study the consequences of nirmatrelvir treatment on antiviral immune responses. To this end, we infected and treated another group of K18-hACE2 transgenic mice exactly as before but monitored them until 24 days p.i. to assess the SARS-CoV-2-specific antibody response in the sera. Because SARS-CoV-2 T cells are not readily detectable in the blood of K18-hACE2 transgenic mice infected with B.1.1.529 (Appendix Fig S2A and B), we decided to subject the mice to a homologous re-challenge with a higher dose (1×10^6 $TCID_{50}$) of aerosolized SARS-CoV-2 B.1.1.529 to evaluate the eventual recruitment of memory T (and B) cells to the infected lung and lung-draining mediastinal lymph nodes (Fig 2A). The mean plasma concentration of nirmatrelvir 4 h after the last administration was 1.40 ± 0.99 μM (Appendix Fig S2C), remarkably similar to the previous experiment. No mice exhibited significant weight loss for the whole duration of the experiment (Fig 2B). Of note, the levels of total IgG specific for the spike S1 subunit (receptor binding domain, RBD) (Fig 2C) and the levels of anti-B.1.1.529-neutralizing antibodies (Fig 2D) were remarkably reduced in nirmatrelvir-treated mice 14 and 21 days p.i., respectively, and 4 days after re-challenge (Fig 2E and F). Consistent with this, B cells recovered from the mediastinal lymph nodes of nirmatrelvir-treated mice 4 days after re-challenge exhibited a lower expression of the activation marker CD95 (Fig 2G), and in one vehicle-treated mouse, we could detect RBD-specific B cells (Fig 2H). Additionally, large lymphocytic aggregates consisting of proliferating B cells were detected in the lungs of vehicle- but not nirmatrelvir-treated mice, 4 days after re-challenge (Appendix Fig S3). SARS-CoV-2-specific $CD8^+$ and $CD4^+$ T cells recovered from lung homogenates were assessed for intracellular IFN-γ and TNF-α expression upon *in vitro* stimulation with a pool of SARS-CoV-2 peptides covering the complete nucleocapsid, membrane, and spike proteins (Silva-Cayetano *et al*, 2021). In line with the results obtained for the humoral response, we found that the frequency and absolute number of IFN-γ^+ and IFN-γ^+ TNF-α^+ SARS-CoV-2-specific $CD8^+$ and $CD4^+$ T cells were significantly lower in the lungs of nirmatrelvir-treated mice compared to vehicle-treated mice, 4 days after homologous re-challenge (Fig 2I–N). Immune responses to SARS-CoV-2 were also reduced when nirmatrelvir treatment was initiated 24 and 48 h after exposure to aerosolized B.1.1.529 (Fig 3A): indeed, we observed a significant reduction in the anti-S1 RBD IgG levels 14 and 21 days p.i. (Fig 3B) and 4 days after heterologous re-challenge with SARS-CoV-2 Omicron subvariant BA.5 (Fig 3C). Similarly, K18-hACE2 transgenic mice infected with the more pathogenic Delta (B.1.617.2) variant (Shuai *et al*, 2022) showed a reduction in humoral responses to SARS-CoV-2 upon nirmatrelvir treatment (Fig 3D and E). Moreover, the expression of the activation marker $CD44^+$ on $CD8^+$ T cells (Fig 3F) and the frequency of granzyme-B^+ and IFN-γ^+ $CD8^+$ T cells were reduced in nirmatrelvir-treated mice compared to vehicle-treated mice (Fig 3G and H). Finally, the negative impact of nirmatrelvir treatment on immune responses to SARS-CoV-2 were also evaluated in C57BL/6 mice infected with a mouse-adapted SARS-CoV-2 (rSARS-2-N501Y$_{MA30}$) (Wong *et al*, 2022) which replicates more robustly and is more

A

B

C

D

E

F

G
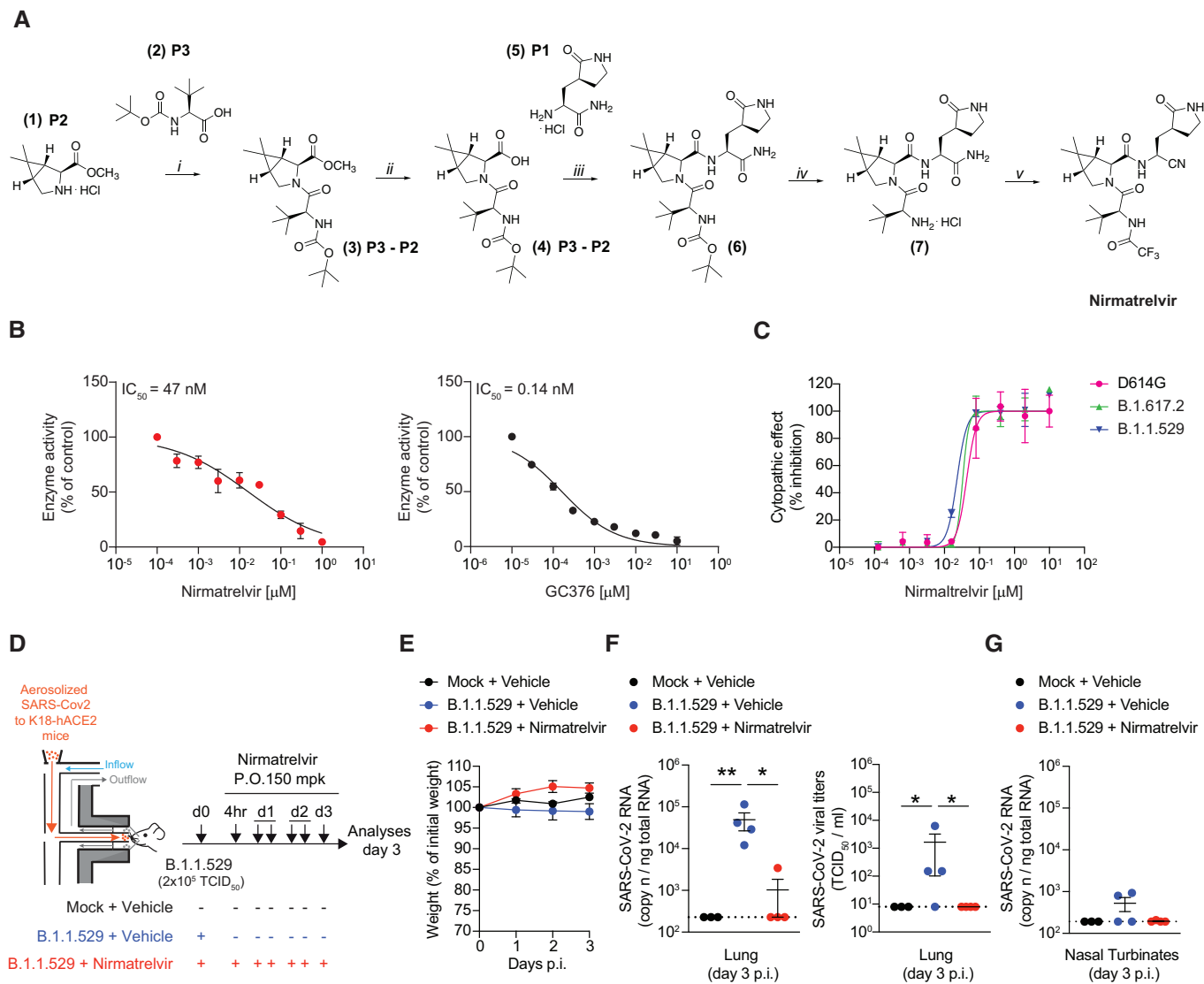
Figure 1. Synthesis of nirmatrelvir and characterization of its biochemical and antiviral activity.

A   Synthesis of nirmatrelvir. Reagents and conditions: (i) HBTU, DIPEA, dry CH_2Cl_2, room temperature (RT), 16 h, 78%; (ii) 1 N aq. LiOH/THF (1:1), RT, 2 h, 100%; (iii) HBTU, DIPEA, dry CH_2Cl_2/DMF, RT, 3 h, 75%; (iv) 4 N HCl in 1,4-dioxane/CH_2Cl_2 (1:1), 0°C to RT, 2 h, 100%; and (v) a: TFAA, dry Py, dry CH_2Cl_2, 0°C to RT, 2 h; b: TFAA, dry Py, dry CH_2Cl_2, 0°C to RT, 15 h, 40% over a and b.

B   Dose-dependent inhibition of nirmatrelvir (left panel) and GC376 (right panel) on SARS-CoV-2 M^{pro}. Prior to adding the substrate for the biochemical reaction, the protease was preincubated for 30 min at 37°C with the indicated concentrations of the compound.

C   Dose-dependent antiviral activity of nirmatrelvir in HEK293T-hACE2 cells infected with SARS-CoV-2 D614G (purple symbols), B.1.617.2 (green symbols), or B.1.1.529 (blue symbols). Antiviral activity was determined as percent inhibition of the virus-induced cytopathic effect.

D   Schematic representation of the experimental setup. Non-anesthetized K18-hACE2 transgenic mice were infected with a target dose of 2×10^5 TCID$_{50}$ of SARS-CoV-2 B.1.1.529 through aerosol exposure (see Materials and Methods for details). Infected mice were treated with 150 mg/kg (mpk) of nirmatrelvir (red symbols, $n = 4$) or vehicle (blue symbols, $n = 4$) six times by oral gavage (P.O.) starting 4 h post-infection (p.i.), and every 12 h thereafter. Mock-treated mice were used as control (black symbols, $n = 3$). Lung, nasal turbinates, and blood were collected and analyzed 3 days p.i.

E   Mouse body weight was monitored daily and is expressed as the percentage of weight relative to the initial weight.

F   Quantification of SARS-CoV-2 RNA (left panel) and viral titers (right panel) in the lung 3 days after infection. RNA values are expressed as copy number per ng of total RNA and the limit of detection is indicated as a dotted line. Viral titers were determined by median tissue culture infectious dose (TCID$_{50}$).

G   Quantification of SARS-CoV-2 RNA in the nasal turbinates 3 days after infection. RNA values are expressed as copy number per ng of total RNA and the limit of detection is indicated as a dotted line.

Data information: Data in B and C represent the mean ± SD of three biological replicates and are representative of three technical replicates; data in E–G are expressed as mean ± SEM and are representative of at least two independent experiments. *P-value < 0.05, **P-value < 0.01; two-way ANOVA followed by Sidak's multiple-comparison test (E); Kruskal–Wallis test followed by uncorrected Dunn's test, each comparison stands alone (F and G).

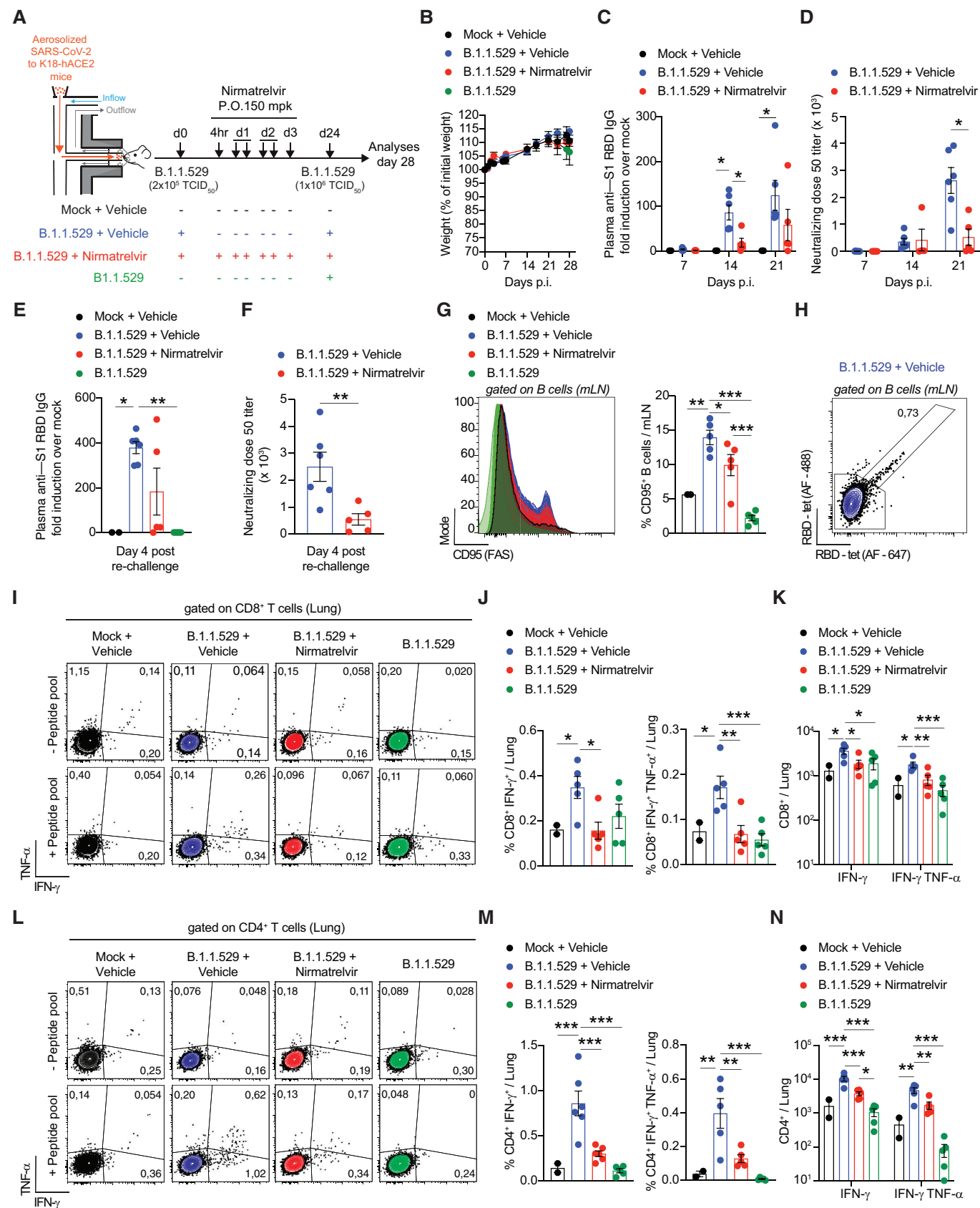Source data are available online for this figure.

Figure 2.

Figure 2. Impact of nirmatrelvir treatment on adaptive immune responses to SARS-CoV-2.

A Schematic representation of the experimental setup. Non-anesthetized K18-hACE2 mice were exposed to a target dose of 2×10^5 $TCID_{50}$ of aerosolized SARS-CoV-2 B.1.1.529 (see Materials and Methods for details). Infected mice were treated with 150 mpk of nirmatrelvir (red symbols, $n = 5$) or vehicle (blue symbols, $n = 6$) for six times by oral gavage (P.O.) starting 4 h p.i., and every 12 h thereafter. Twenty-four days after infection, mice were re-challenged with a target dose of 1×10^6 $TCID_{50}$ of SARS-CoV-2 B.1.1.529 through aerosol exposure. Mock-treated mice were used as non-infected controls (black symbols, $n = 3$). A group of naïve mice challenged with 1×10^6 $TCID_{50}$ of SARS-CoV-2 B.1.1.529 served as additional controls (green symbols, $n = 5$). Blood was collected 7, 14, and 21 days after the first infection and 4 days post-re-challenge. Lung, nasal turbinates, and lung-draining mediastinal lymph nodes (mLN) were collected and analyzed 4 days post-re-challenge.

B Mouse body weight was monitored daily and is expressed as percentage of weight relative to the initial weight.

C–F Quantification of anti-S1 RBD IgG levels by ELISA in the plasma of the indicated mice (C) 7, 14, and 21 days p.i. or (E) 4 days post-re-challenge. Neutralization dose 50 (ND50) against SARS-CoV-2 B.1.1.529 pseudovirus in the plasma of the indicated mice (D) 7, 14, and 21 days p.i. or (F) 4 days post-re-challenge.

G Flow cytometry histogram (left panel) and percentage (right panel) of B cells stained positive for CD95 in the mLN of the indicated mice 4 days post-re-challenge (pre-gated on live$^+$/CD4$^-$/CD8$^-$/B220$^+$/CD19$^+$ cells).

H Flow cytometry plot of RBD-specific B cells detected by two fluorescently labeled streptavidin-based RBD-biotinylated tetramers in the mLN of one vehicle-treated mouse 4 days post-re-challenge (pre-gated on live$^+$/CD4$^-$/CD8$^-$/B220$^+$/CD19$^+$ cells).

I–N Representative flow cytometry plots of (I) CD8$^+$ T cells or (L) CD4$^+$ T cells expressing IFN-γ and TNF-α in the lungs of the indicated mice 4 days post-re-challenge. Unstimulated cells are shown in the upper panels, whereas cells re-stimulated with a pool of SARS-CoV-2 peptides for 4 h at 37°C are shown in the bottom panels. Plots were pre-gated as (I) live$^+$/B220$^-$/CD19$^-$/CD4$^-$/CD8$^+$ cells or (L) live$^+$/B220$^-$/CD19$^-$/CD8$^-$/CD4$^+$. Frequency (J, M) and absolute number (K, N) of IFN-γ- and TNF-α-producing CD8$^+$ T cells (J, K) or CD4$^+$ T cells (M, N) in the lung of the indicated mice 4 days post-re-challenge.

Data information: Data are expressed as mean ± SEM and are representative of at least two independent experiments. *P-value < 0.05, **P-value < 0.01, ***P-value < 0.001; two-way ANOVA followed by Sidak's multiple-comparison test (B–D); Kruskal–Wallis test followed by uncorrected Dunn's test, each comparison stands alone (E); Mann–Whitney test (F); and one-way ANOVA followed by uncorrected Fisher's LSD, each comparison stands alone (G, J, K, M, N). Normal distribution was verified by Shapiro–Wilk test.

Source data are available online for this figure.

pathogenic than B.1.1.529, yet maintains its sensitivity to nirmatrelvir (Appendix Fig S4A–D). Consistent with previous results, the levels of total IgG specific for the spike RBD were remarkably reduced in C57BL/6 mice that were treated with nirmatrelvir 1 day after infection with rSARS2-N501Y$_{MA30}$ (Fig 3I and J).

Nirmatrelvir treatment of mice infected with unrelated viruses (i.e., vesicular stomatitis virus [VSV] and lymphocytic choriomeningitis virus [LCMV]) did not inhibit the development of antiviral adaptive immune responses, indicating that nirmatrelvir is not *per se* an immune suppressive drug (Appendix Fig S5).

Of note, we did not detect viral titers in the lungs of all but one nirmatrelvir-treated mouse after homologous re-challenge (Appendix Fig S6A and B). Similarly, infection of K18-hACE2 transgenic mice

with the poorly pathogenic Omicron (B.1.1.529) variant (Halfmann *et al*, 2022) did not allow us to evaluate clinical signs of disease. We believe that the failure to observe decreased protection upon re-infection in mice treated with nirmatrelvir (despite a prominent reduction in adaptive immunity) has to do with the limitations of the experimental setup. Case in point, we infected mice with Omicron (B.1.1.529) variant, we treated or not with nirmatrelvir and we re-challenged mice with Delta (B1.1.617) variant, known to be more pathogenic and to replicate at higher levels in mice (Shuai *et al*, 2022). As shown in Appendix Fig S6C and D, two of six mice that were treated with nirmatrelvir during the primary infection showed higher viral RNA in the lungs upon Delta re-challenge. Future studies with different SARS-CoV-2 variants and/or doses

Figure 3. Nirmatrelvir treatment of SARS-CoV-2-infected mice blunts the development of antiviral adaptive immune responses independent of timing of treatment and viral variant.

A Schematic representation of the experimental setup. Non-anesthetized K18-hACE2 mice were exposed to a target dose of 2×10^5 $TCID_{50}$ of aerosolized SARS-CoV-2 B.1.1.529. Infected mice were treated with 150 mpk of nirmatrelvir (red symbols, $n = 5$) or vehicle (blue symbols, $n = 4$) six times by oral gavage (P.O.) starting 24 h p.i. (full-red symbols, $n = 5$) or 48 h p.i. (empty-red symbols, $n = 5$), and every 12 h thereafter. Thirty-eight days after infection, mice were re-challenged with a target dose of 1×10^6 $TCID_{50}$ of SARS-CoV-2 BA.5 through aerosol exposure. Mock-treated mice were used as non-infected controls (black symbols, $n = 3$).

B, C Quantification of anti-S1 RBD IgG levels by ELISA in the plasma of the indicated mice (B) 14 and 21 days p.i. and (C) 4 days post-re-challenge.

D Schematic representation of the experimental setup. Non-anesthetized K18-hACE2 mice were exposed to a target dose of 2×10^5 $TCID_{50}$ of aerosolized SARS-CoV-2 B.1.617.2. Infected mice were treated with 150 mpk of nirmatrelvir (red symbols, $n = 3$) or vehicle (blue symbols, $n = 4$) for six times by oral gavage (P.O.) starting 24 h p.i., and every 12 h thereafter. Mock-treated mice were used as non-infected controls (black symbols, $n = 2$).

E Quantification of anti-S1 RBD IgG levels by ELISA in the plasma of the indicated mice 7 days p.i.

F Flow cytometry histogram (left panel) and geometric mean fluorescent intensity (gMFI) quantification (right panel) of CD44 expression by CD8$^+$ T cells in the blood of the indicated mice 7 days p.i. (pre-gated on live$^+$/ B220$^-$/ CD19$^-$/ CD4$^-$/ CD8$^+$ cells).

G, H Frequency of (G) granzyme-B- and (H) IFN-γ-producing CD8$^+$ T cells in the blood of the indicated mice 7 days p.i. Cells were stimulated *in vitro* with a pool of SARS-CoV-2 peptides for 4 h at 37°C. Plots were pre-gated as above.

I Schematic representation of the experimental setup. Non-anesthetized C57BL/6 mice were exposed to a target dose of 1×10^5 $TCID_{50}$ of aerosolized rSARS-N501Y$_{MA30}$. Infected mice were treated with 150 mpk of nirmatrelvir (red symbols, $n = 4$) or vehicle (blue symbols, $n = 4$) six times by oral gavage (P.O.) starting 24 h p.i., and every 12 h thereafter. Mock-treated mice were used as non-infected controls (black symbols, $n = 3$).

J Quantification of anti-S1 RBD IgG levels by ELISA in the plasma of the indicated mice 7, 14, and 21 days p.i.

Data information: Data are expressed as mean ± SEM. *P-value < 0.05, **P-value < 0.01, ***P-value < 0.001; One-way ANOVA followed by uncorrected Fisher's LSD, each comparison stands alone. Normal distribution was verified by Shapiro–Wilk test.
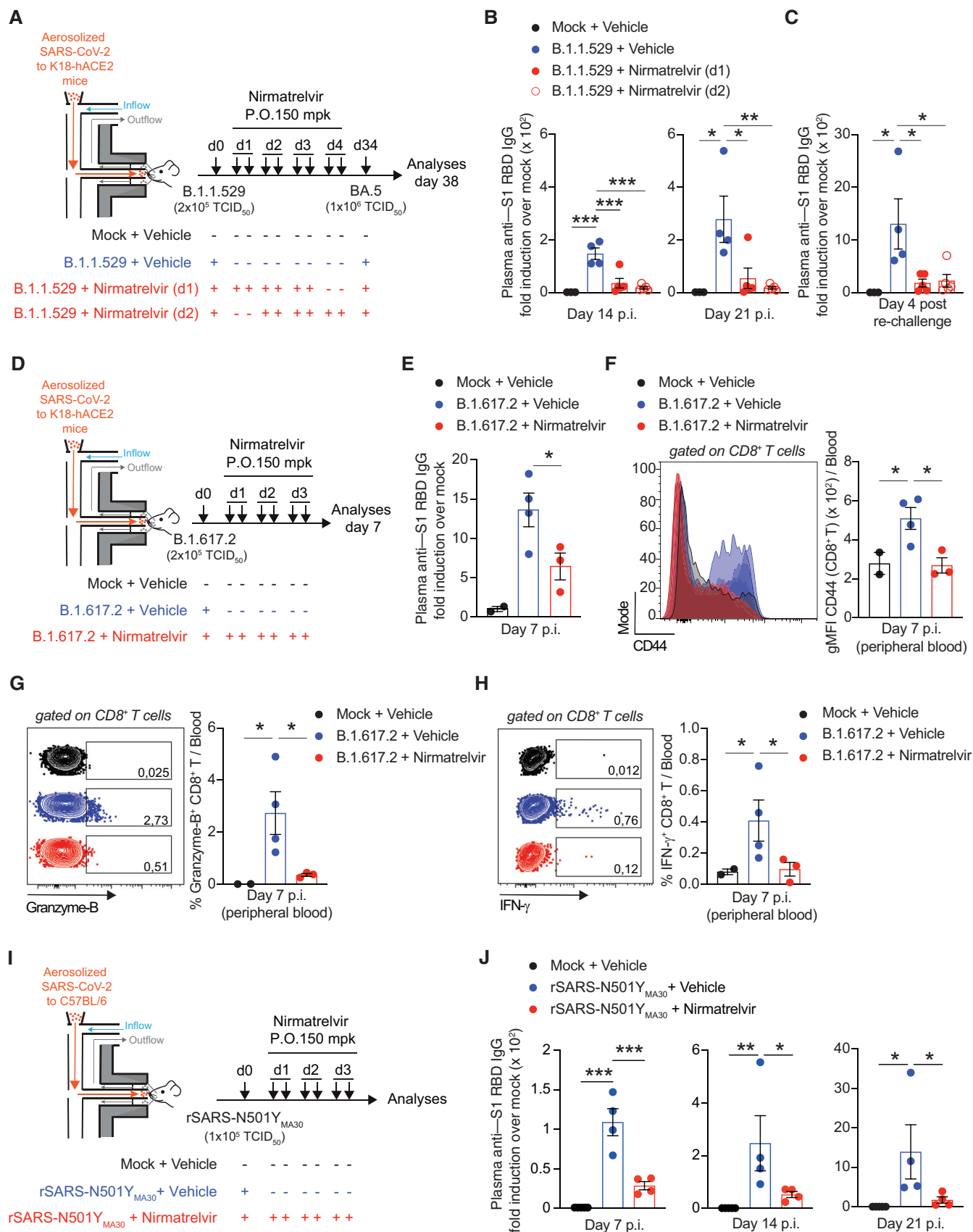
Source data are available online for this figure.Figure 3.

Figure 3.

should assess the impact of the reduced adaptive immunity caused by nirmatrelvir treatment on viral load and the severity of disease progression upon re-challenge.

In summary, our results indicate that nirmatrelvir treatment negatively impacts the development of adaptive immune response to SARS-CoV-2 in mice. Although the mechanistic bases behind this observation were not addressed in this study, it is conceivable that this is due to insufficient antigen exposure (quantity and/or duration) of naïve B and T cells. It is worth noting that successful antimicrobial treatment does not inevitably result in reduced adaptive immune responses to any pathogen. For instance, treatment of mice infected with *Listeria monocytogenes* with amoxicillin early after infection did not significantly impair the development of T cell responses (Mercado *et al*, 2000; Corbin & Harty, 2004). Furthermore, treatment with antibiotics before *L. monocytogenes* infection allowed the development of functional antigen-specific memory CD8$^+$ T cells in the absence of contraction (Badovinac *et al*, 2004). In addition, monoclonal antibody therapy with bamlanivimab during acute COVID-19 did not impact the development of a robust antiviral T cell response (Ramirez *et al*, 2022). Thus, the effect of antiviral therapy on adaptive immunity probably depends on the impact of such treatment on several factors including not only pathogen replication but also duration of antigen expression and presentation, activation of innate immunity, etc.

While the clinical data continue to support nirmatrelvir treatment for the prevention of severe COVID-19 in high-risk individuals (Hammond *et al*, 2022), the data reported here draw attention to a potential negative impact of this therapy. Whether this effect is an exclusive feature of nirmatrelvir or whether forthcoming antivirals acting on SARS-CoV-2 would have similar effects should be addressed in future studies. Although mice do not reproduce the viral rebound observed in some patients treated with nirmatrelvir, we believe that our results might help explain the virological and/or symptomatic relapse after treatment completion reported in some individuals and should inform clinical and public health policies.

Materials and Methods

Viruses

The SARS-CoV-2 isolates were propagated in Vero E6-hTMPRSS2 cells. Briefly, 3×10^6 Vero E6-hTMPRSS2 cells were plated into T75 flask in DMEM 2% FBS. After 24 h, cells were inoculated with 0.001 or 0.01 MOI of SARS-CoV-2 D614G (hCoV-19/Italy/LOM-UniMI-vir1/2020; EPI_ISL_58405), SARS-CoV-2 B.1.617.2 (hCoV-19/Italy/LOM-Milan-UNIMI9615/2021, EPI_ISL_3073880), SARS-CoV-2 B.1.1.529 (hCoV-19/Italy/LOM-19182/2021, EPI_ISL_10898045), SARS-CoV-2 Omicron subvariant B5 (hCoV-19/Italy/LOM-Unimi-5882/2022, EPI_ISL_14036188), and mouse-adapted SARS-CoV-2 (rSARS2-N501Y$_{MA30}$) (Wong *et al*, 2022). Supernatant was collected 48–72 h later, centrifuged for 5 min at 500 *g*, aliquoted, and stored at −80°C.

VSV Indiana and LCMV WE were propagated and quantified as described (Sammicheli *et al*, 2016; Giovanni *et al*, 2020).

Nirmatrelvir synthesis

Reagents and solvents were purchased from commercial sources and used without further purification. Reactions were carried out at room temperature (RT), unless otherwise specified. Moisture-sensitive reactions were performed under a positive pressure of dry nitrogen in oven-dried glassware. Analytical thin-layer chromatography (TLC) on silica gel 60 F254 plates (250 μm thickness) was performed to monitor the reaction progress, using UV and KMnO$_4$ as revelation method. Analytical HPLC was performed to monitor the reaction progress and the purity of target compound. Flash chromatography on silica gel (70—230 mesh) and preparative HPLC were performed for purification. All products were characterized by their NMR and MS spectra. (ESI)-MS spectra were performed on a LTQ Orbitrap XL mass spectrometer (Thermo Fisher Scientific) by infusion into the ESI source using MeOH as solvent. ^{1}H NMR spectra were recorded in deuterated solvents at 25°C on Bruker Avance NEO 400 MHz and 700 MHz instruments. equipped with a RT-DR-BF/1H-5 mm-OZ SmartProbe. Chemical shifts (δ) are reported in part per million (ppm) downfield from tetramethylsilane, using residual solvent signal as the internal reference.

The final compound was characterized by HPLC-MS/MS, using a Dionex ULTIMATE 3000 (Thermo Fisher Scientific) HPLC module and a LTQ XL mass spectrometer with electrospray ionization in positive mode and an Ion-Trap detector. Separation was performed with a Kinetex column C18 Polar column (250 mm × 4.6 mm; particle size 5 μm, Phenomenex, Torrance, CA, USA) at 30°C, using a 17 min gradient, 5% [0.1% TFA/CH$_3$CN]/95% [0.1% TFA/H$_2$O] to 95% [0.1% TFA/CH$_3$CN]. Analytical HPLC was performed on Shimatzu-1100 HPLC using a Kinetex C18 column (4.6 mm × 150 mm, 5 μm, 100 Å) with an acetonitrile (0.1% HCOOH)−water (0.1% HCOOH) custom gradient. The purity of the final compound was > 95%, as determined by HPLC (UV λ = 200 nm). Preparative HPLC was performed on Shimatzu LC-20AP using a Sunfire C18 column (19 mm × 100 mm, 5 μm, 100 Å) with an acetonitrile (0.1% HCOOH)−water (0.1% HCOOH) custom gradient.

Briefly, two "building blocks," the acid dipeptide P3-P2 and the residue P1, were first synthesized separately and then assembled to generate the advanced intermediate 6. 6 was deprotected to obtain intermediate 7 that was converted into the final product nirmatrelvir with one pot two steps procedure by converting 7 primary amide in P1 to the nitrile, electrophilic "warhead", and obtaining the trifluoroacetamide, as N terminal capping group.

Methyl (1R,2S,5S)-3-((S)-2-((tert-butoxycarbonyl)amino)-3, 3-dimethylbutanoyl)-6, 6-dimethyl-3-azabicyclo[3.1.0]hexane-2-carboxylate (3). Tert-leucine-OH 2 (1 g, 4.32 mmol) was dissolved in dry CH$_2$Cl$_2$ (5 ml), and amine hydrochloride 1 (1.15 g, 5.62 mmol), HBTU (1.8 g, 4.75 mmol), and DIPEA (1.5 ml, 8.64 mmol) were added at 0°C under a nitrogen atmosphere. The resulting solution was kept under magnetic stirring at RT for 16 h. Then, the reaction mixture was washed with saturated aq. NaHCO$_3$ (x1), 1 N HCl (x1), and brine (x1), dried over anhydrous Na$_2$SO$_4$, filtered, and concentrated under vacuum. The reaction crude was purified by flash column chromatography (Hexane / EtOAc 8: 2) to obtain a colorless oil (reaction time: 16 h; yield: 1.38 g, 78%). ^{1}H NMR (400 MHz, DMSO-d$_6$) δ 6.73 (d, *J* = 9.3 Hz, 1H), 4.21 (s, 1H), 4.05 (d, *J* = 9.4 Hz, 1H), 3.93 (d, *J* = 10.4 Hz, 1H), 3.79 (dd, *J* = 10.3, 5.3 Hz, 1H), 3.65 (s, 3H), 1.55–1.49 (m, 1H), 1.41 (d, *J* = 7.5 Hz, 1H), 1.35 (s, 9H), 1.01 (s, 3H), 0.93 (s, 9H), 0.85 (s, 3H). MS (ESI) *m/z* calcd: [M + H]$^+$ for C$_{20}$H$_{35}$N$_2$O$_5^+$ 383.51, found [M + H]$^+$ 383.50.

(1R,2S,5S)-3-((S)-2-((tert-butoxycarbonyl)amino)-3, 3-dimethyl butanoyl)-6, 6-dimethyl-3-azabicyclo[3.1.0]hexane-2-carboxylic acid

(4). The methyl ester intermediate 3 (1.35 g 3.6 mmol) was dissolved in THF (18 ml), then 1 N aq. LiOH was added (18 mmol, 18 ml), and the reaction mixture was kept under stirring at RT for 3 h. The reaction mixture was cooled to 0°C, placed in water / ice, acidified with 1 N HCl to pH = 4, then extracted with EtOAc (x3). Then, the collected organic layers were washed with brine (x1), dried over Na_2SO_4, filtered and concentrated under vacuum to afford dipeptide acid 4 as white solid which was used in the following step without further purification (reaction time: 2 h, yield: 1.30 mg, 100%). ^{1}H NMR (400 MHz, DMSO-d_6) δ 12.54 (s, 1H), 6.67 (d, J = 9.4 Hz, 1H), 4.13 (s, 1H), 4.04 (s, 1H), 3.91 (d, J = 10.4 Hz, 1H), 3.77 (dd, J = 10.2, 5.3 Hz, 1H), 1.54–1.46 (m, 1H), 1.40 (s, 1H), 1.35 (s, 9H), 1.01 (s, 3H), 0.93 (s, 9H), 0.84 (s, 3H). MS (ESI) m/z calcd: $[M + H]^+$ for $C_{19}H_{33}N_2O_5^+$ 369.48, found $[M + H]^+$ 369.50.

Tert-butyl ((S)-1-((1R,2S,5S)-2-(((S)-1-amino-1-oxo-3-((S)-2-oxopyrrolidin-3-yl)propan-2-yl)carbamoyl)-6, 6-dimethyl-3-azabicyclo[3.1.0]hexan-3-yl)-3, 3-dimethyl-1-oxobutan-2-yl)carbamate (6). Dipeptide acid 4 (1.22 g, 3.3 mmol) was dissolved in dry CH_2Cl_2 (6 ml) and the amine hydrochloride 5 (898 mg, 4.3 mmol), HBTU (1.25 g, 3.6 mmol), and DIPEA (1.4 ml, 8.25 mmol) were added at 0°C, then DMF (3 ml) was added, and the reaction mixture was kept under stirring at RT for 3 h. The reaction mixture was washed with 1 N HCl (x3), saturated aq. $NaHCO_3$ (x3), brine (x3), dried over Na_2SO_4, filtered, and concentrated under vacuum. The crude was purified by flash chromatography ($CHCl_3$/MeOH 5 to10%) to obtain the tripeptide 6 as a white solid (reaction time: 3 h, yield: 1.3 g, 75%). ^{1}H NMR (400 MHz, DMSO-d_6) δ 9.41 (d, J = 8.6 Hz, 1H), 8.29 (d, J = 8.9 Hz, 1H), 7.55 (s, 1H), 7.31 (s, 1H), 7.03 (s, 1H), 4.43 (d, J = 8.6 Hz, 1H), 4.35–4.25 (m, 2H), 3.91–3.84 (m, 1H), 3.67 (d, J = 10.4 Hz, 1H), 3.13 (t, J = 9.0 Hz, 1H), 3.06–2.97 (m, 1H), 2.45–2.34 (m, 1H), 2.14 (dt, J = 10.5, 7.4 Hz, 1H), 1.97–1.86 (m, 1H), 1.70–1.57 (m, 1H), 1.54–1.45 (m, 2H), 1.38 (d, J = 7.7 Hz, 1H), 1.10 (s, 3H), 1.05 (s, 9H), 0.98 (s, 9H), and 0.84 (s, 3H). MS (ESI) m/z calcd: $[M + H]^+$ for $C_{26}H_{44}N_5O_6^+$ 522.67, found $[M + H]^+$ 522.70.

(1R,2S,5S)-N-((S)-1-cyano-2-((S)-2-oxopyrrolidin-3-yl)ethyl)-3-((S)-3, 3-dimethyl-2-(2, 2, 2-trifluoroacetamido)butanoyl)-6, 6-dimethyl-3 azabicyclo[3.1.0]hexane-2-carboxamide (nirmatrelvir). Tripeptide intermediate 6 (300 mg, 0.57 mmol) was dissolved in CH_2Cl_2 (3 ml), the solution was cooled to 0°C, 4 N HCl d in 1,4-dioxane (1.5 ml, 5.7 mmol), and the reaction mixture was stirred at RT for 2 h. Then, the solvent mixture was evaporated in vacuo and the crude was treated with hexane to obtain the desired compound 7 as HCl salt white solid, which was used without further purification in the following step (reaction time: 2 h, yield: 261 mg, 100%). Intermediate 7 (230 mg, 0.5 mmol) was suspended in dry CH_2Cl_2 (2 ml), under an N_2 atmosphere, and dry pyridine (0.10 ml, 1.43 mmol) was added. After 30 min, the resulting mixture was cooled to 0°C, TFFA (0.08 ml, 0.57 mmol) was added, and the reaction mixture was kept under stirring at RT for 2 h. The complete conversion of the intermediate 7 was monitored by TLC, then anhydrous pyridine (0.18 ml, 2.28 mmol) was added, and the mixture was cooled at −5°C. After 5 min, TFFA (0.16 ml, 1.14 mmol) was added and the reaction was kept under stirring at RT for 18 h. The solvent was removed under vacuum, the resulting crude was diluted with EtOAc, and the organic phase was washed with 0.5 N HCl (x3), saturated aq. $NaHCO_3$ (x1), dried over anhydrous Na_2SO_4,

filtered, and concentrated under vacuum. The crude was purified by preparative HPLC (Shimadzu LC-20AP; column: Sunfire, 5 μm, C18, 100 Å, 19 × 100 mm, C18 with TMS end capping; mobile phase gradient: 30–75, 20 min [H_2O 0.1% HCOOH, MeCN 0.1% HCOOH]; time course: 20 min; t_R = 7.8 min) to afford the target nirmatrelvir (yield: 115 mg, 40%) as a white solid. ^{1}H NMR (600 MHz, DMSO-d_6) δ 9.43 (d, J = 8.4 Hz, 1H), 9.03 (d, J = 8.6 Hz, 1H), 7.68 (s, 1H), 4.97 (ddd, J = 10.9, 8.6, 5.1 Hz, 1H), 4.41 (d, J = 8.4 Hz, 1H), 4.15 (s, 1H), 3.91 (dd, J = 10.4, 5.5 Hz, 1H), 3.69 (d, J = 10.4 Hz, 1H), 3.17–3.11 (m, 1H), 3.04 (td, J = 9.4, 7.1 Hz, 1H), 2.40 (tdd, J = 10.4, 8.4, 4.4 Hz, 1H), 2.14 (ddd, J = 13.4, 10.9, 4.4 Hz, 1H), 2.11–2.03 (m, 1H), 1.76–1.65 (m, 2H), 1.57 (dd, J = 7.6, 5.5 Hz, 1H), 1.32 (d, J = 7.6 Hz, 1H), 1.03 (s, 3H), 0.98 (s, 9H), and 0.85 (s, 3H). MS (ESI) m/z calcd: $[M + H]^+$ for $C_{23}H_{33}F_3N_5O_4^+$ 500.53, found $[M + H]^+$ 500.40.

The image of ^{1}H NMR and MS spectra of nirmatrelvir are reported in Appendix Figs S7 and S8.

Biochemical assay

M^{pro} SARS-CoV-2 was expressed in *E. coli* cells BL21 (DE3) and purified as described (Costanzi *et al*, 2021; Kuzikov *et al*, 2021). Briefly, the protein was purified in two steps using a Ni-Sepharose column and by HiTrap Q HP column and the fractions containing the M^{pro} SARS-2 were pooled and concentrated using Amicon Ultra 15 centrifugal filters, at 4,000 *g*, at 4°C, in a buffer exchange (20 mM Tris–HCl, 150 mM NaCl, 1 mM EDTA, and 1 mM DTT, pH 7.8). Protein purity was verified by SDS–PAGE analysis and the proteins were stored at −80°C.

The M^{pro} SARS-CoV-2 biochemical assays was performed in 386 wells plate in 20 μl of assay buffer containing diluted protein, 20 mM Tris (pH 7.3), 100 mM NaCl, and 1 mM EDTA, with the addition of 5 mM TCEP, 0.1% BSA. In Fig 1B, the protein was preincubated for 30 min at 37°C with different concentrations of nirmatrelvir or GC376, a commercially available broad-spectrum M^{pro} inhibitor (*17–20*). The substrate DABCYL-KTSAVLQ↓SGFRKM-EDANS (Bachem) was added, and the generation of the fluorescent product was monitored after 15 min of incubation (Ex 340 nm, Em 490 nm). In Appendix Fig S1A, the protein and the compound were not preincubated and the enzymatic reaction was immediately initiated with the addition of the substrate in the assay buffer, as described (Owen *et al*, 2021). The reaction was allowed to progress for 60 min at 23°C and then monitored (Ex 340 nm, Em 490 nm). Dose–response curve were generated by non-linear regression curve fitting with GraphPad Prism to calculate IC_{50}.

In vitro antiviral assays

For *in vitro* antiviral assay, HEK293T-hACE were plated in 96-well plates at 5,000 cells/well in complete DMEM plus 2% FBS. After 24 h, cells were treated with seven concentrations of fivefold serially diluted nirmatrelvir and infected at 0.1 MOI of SARS-CoV-2 virus. DMSO was used as vehicle for compound serial dilution and not treated control (final concentration 0.25%). Not infected condition was inserted as negative control of infection. Each condition was assayed in three replicates. Antiviral activity was evaluated by qPCR quantification of secreted SARS-CoV-2 RNA and/or by

cytopathic effect protection assay (CPE) after 72 h of incubation at 37°C under 5% CO_2.

For the quantification of SARS-CoV-2 RNA by qPCR, 10 μl of cell supernatants were subjected to direct lysis with the addition of 10 μl ViRNAex solution (Cabru) and heated at 70°C for 15 min. After addition of distilled water (1:1), samples were used as template for PCR amplification using TaqPath™ 1-Step RT-qPCR Master Mix (Thermo Fisher Scientific) and specific SARS-CoV-2 primers/probe (2019-nCoV RUO Integrated DNA Technologies). Obtained Ct were normalized to untreated infected wells, and dose–response curve were generated by non-linear regression curve fitting with GraphPad Prism to calculate the concentration that inhibits 50% of viral replication (IC_{50}).

For CPE assays, CellTiter-Glo® Luminescent Cell Viability Assay (Promega), was used. Relative luciferase units (RLUs) were normalized to infected or uninfected controls in order to obtain the percentage of inhibition of cytopathic effect using the following formula: % CPE inhibition = 100*(Test Cmpd − Avg. Virus)/(Avg. Cells − Avg. Virus), where Avg. virus is the RLU average obtained from infected and not treated wells, while Avg. cells is the RLU average obtained from not infected and not treated wells. Dose–response curve was generated by non-linear regression curve fitting with GraphPad Prism to calculate IC_{50}.

Mice

B6.Cg-Tg(K18-ACE2)^{2Prlmn}/J mice (referred to in the text as K18-hACE2) were purchased from The Jackson Laboratory. C57BL/6 mice were purchased from Charles River. Mice were housed under specific pathogen-free conditions, and heterozygous mice were used at 8–10 weeks of age. All experimental animal procedures were approved by the Institutional Animal Committee of the San Raffaele Scientific Institute and all infectious work was performed in designed BSL-3 workspaces.

Mouse infection

Infection of K18-hACE2 transgenic mice with aerosolized SARS-CoV-2 was performed as described (Fumagalli et al, 2021). Briefly, non-anesthetized K18-hACE2 mice were placed in a nose-only Allay restrainer on the inhalation chamber (DSI Buxco respiratory solutions, DSI). To reach a target accumulated inhaled aerosol (also known as delivered dose) of 2×10^5 TCID50 mice were exposed to aerosolized SARS-CoV-2 B.1.1.529 or B.1.617.2 for 30–60 min (depending on the total volume of diluted virus and on the number of mice simultaneously exposed). In selected experiments, mice were exposed to a target accumulated inhaled aerosol of 1×10^6 TCID50. In Fig 3I and J, and Appendix Fig S4, C57BL/6 mice were exposed to a target dose of 1×10^5 TCID50 of the mouse-adapted SARS-CoV-2 strain (rSARS-N501Y$_{MA30}$). Primary inflows and pressure were controlled and set to 0.5 l/min/port and −0.5 cm H_2O, respectively. As control, K18-hACE2 mice or C57BL/6 mice received the same volume of aerosolized PBS (125 μl per mouse). Infected mice were monitored daily to record body weight, and clinical and respiratory parameters.

C57BL/6 WT mice were infected intravenously with 1×10^6 plaque-forming units (pfu) of VSV Indiana and 2.5×10^6 pfu of LCMV WE.

In vivo treatment

K18-hACE2 mice were treated by oral gavage with nirmatrelvir at 150 mg/kg or vehicle (0.5% Methylcellulose (Methocel A4M, Sigma #94378) and 2% Tween80 (Sigma #8170611000) in purified water) for six times starting 4 h post-infection, and every 12 h thereafter. In selected experiments, K18-hACE2 mice or C57BL/6 mice were treated with nirmatrelvir starting 1 or 2 days post-infection (Fig 3).

LC–MS/MS analysis

The nirmatrelvir stock solutions were prepared in DMSO at 1 mg/ml and further diluted to obtain a working solution (WS) at 20 μg/ml. The drug JWH-250 was used as internal standard. The internal standard working solutions (IS-WS) was prepared at 20 ng/ml in methanol:acetonitrile (50:50, v/v) acidified with 0.1% formic acid.

Plasma of mice were collected, centrifuged at 10,621 g for 10 min, and incubated at 60°C for 30 min. The mixture of 30 μl of plasma, 105 μl of IS-WS, and 15 μl of WS was vortex for 1 min and centrifuged at 12,500 g for 10 min at 4°C. The supernatant was collected and 100 μl were injected into the liquid chromatography tandem mass spectrometry (LC–MS/MS) system. The HPLC equipment consisted of an LC AC System from AB Sciex (Toronto, ON, Canada). A Triple Quadrupole Mass Spectrometer (API 2000) from AB-Sciex (Toronto, ON, Canada) was used for detection. The analytes were separated using an Acquity UPLC BEH C18 1.7 μm Column (2.1 × 50 mm ID) from Waters. The mobile phases were (B) MeOH containing 0.2% formic acid and (A) water containing 0.1% formic acid, at a flow rate of 0.4 ml/min, and were entirely transferred into the mass spectrometer source. The gradient elution was as follows: increase in the organic phase from 10 to 100% in 2 min and after 1.5 min of 100% B, the column was led to the original conditions; equilibration of the column was achieved in 2 min. Both analytes were detected in positive ionization with a capillary voltage of 4,500 V, nebulizer gas (air) at 45 psi, turbo gas (nitrogen) at 70 psi, and 450°C. The other ion source parameters were set as follows: curtain gas (CUR) 25 psi; collision gas (CAD) 6 psi; declustering potential 80 V; and entrance potential 8 V. Instrument conditions optimization was performed by direct infusion and manual tuning. Data collection and elaboration were performed by means of Analyst 1.4 software (AB- Sciex). The quantitative data were acquired using multi reaction monitoring (MRM) mode. Two MRM transitions (precursor ion > fragment ion) were selected for the analytes. The parameters used for each analyte are listed in the Appendix Table S1.

The analytical method was validated according to FDA guidelines for bioanalytical method validation. Linearity, precision, accuracy, limits of detection (LODs), and limits of quantification (LOQ) were evaluated. Calibration standard solutions were prepared in blank plasma by spiking 15 μl of a standard mixture at appropriate concentration to 30 μl of plasma and by adding 105 μl of methanol:acetonitrile (50:50, v/v). Calibrators were then treated similarly to the animal samples. The calibration range was 2–750 ng/ml and the calibrators were prepared at nine level of concentration. Precision, recovery, and accuracy were evaluated at three level of concentrations (25, 100, and 750 ng/ml) and resulted within the acceptable limits. LOD was defined as the lowest concentration with a signal-to-noise (S/N) ratio greater than 3. LOQ was defined as the

concentration at which both precision (RSD %) and accuracy were less than 20%. LOQ resulted to be 2 ng/ml, while LOD was 1 ng/ml for both analytes.

Tissue homogenate and viral titers

Tissues homogenates were prepared by homogenizing perfused lungs using gentleMACS Octo Dissociator (Miltenyi BioTec, #130-096-427) in M tubes (#130-093-335) containing 1 ml of DMEM 0% FBS. Samples were homogenized for three times with program m_Lung_01_02 (34 s, 164 rpm). The homogenates were centrifuged at 2,000 *g* for 5 min at 4°C. The supernatant was collected and stored at −80°C for viral isolation and viral load detection. Viral titer was calculated by 50% tissue culture infectious dose (TCID$_{50}$). Briefly, Vero E6 cells were seeded at a density of 1.5×10^4 cells per well in flat-bottom 96-well tissue culture plates. The following day, 10-fold dilutions of the homogenized tissue were applied to confluent cells and incubated 1 h at 37°C. Then, cells were washed with phosphate-buffered saline (PBS) and incubated for 72 h at 37°C in DMEM 2% FBS. Cells were fixed with 4% paraformaldehyde for 30 min and stained with 0.05% (wt/vol) crystal violet in 20% ethanol. Limit of detection (LOD) was defined as the lowest concentration whereby the virus, used as positive control, has killing capacity of cells.

RNA extraction and qPCR

Tissues homogenates were prepared by homogenizing perfused lung and nasal turbinates using gentleMACS dissociator (Miltenyi BioTec, #130-096-427) with program RNA_02 in M tubes (#130-096-335) in 1 ml of Trizol (Invitrogen, #15596018). The homogenates were centrifuged at 2,000 *g* for 1 min at 4°C and the supernatant was collected. RNA extraction was performed by combining phenol/guanidine-based lysis with silica membrane-based purification. Briefly, 100 μl of chloroform was added to 500 μl of homogenized sample and total RNA was extracted using ReliaPrep™ RNA Tissue Miniprep column (Promega, Cat #Z6111). Total RNA was isolated according to the manufacturer's instructions. qPCR was performed using TaqMan Fast virus 1 Step PCR Master Mix (Life Technologies #4444434), standard curve was drawn with 2019_nCOV_N Positive control (IDT#10006625), and primers used are as follows: 2019-nCoV_N1- Forward Primer (5′-GAC CCC AAA ATC AGC GAA AT-3′), 2019-nCoV_N1- Reverse Primer (5′-TCT GGT TAC TGC CAG TTG AAT CTG-3′), and 2019-nCoV_N1-Probe (5′-FAM-ACC CCG CAT TAC GTT TGG TGG ACC-BHQ1-3′) (Centers for Disease Control and Prevention (CDC) Atlanta, GA 30333). All experiments were performed in duplicate.

ELISA

Individual sera were titrated in parallel for the presence of SARS-CoV-2 S1 RBD-specific antibody by end-point ELISA. The ELISA plates were functionalized by coating with recombinant Sars-CoV-2 S1 subunit protein (RayBiotech, #230-30162) at a concentration of 2 μg/ml and incubated overnight (O/N) at 4°C. Subsequently, the plates were blocked with 3% fat-free milk and 0.05% Tween20 in PBS for 1 h at RT. The sera were then added at a dilution of 1/20 (sera from day 7) or 1/500 (sera from day 14, 21, and 28) and

diluted 1:10 up to 1/1,280 or 1/32,000, respectively, in duplicate, and the plates were incubated for 2 h at RT. After five washes with 0.05% Tween20 in PBS, the secondary anti-murine IgG conjugated with horseradish peroxidase (HRP, PerkinElmer, #NEF822001EA) (1:2,000) was added and the plates were incubated for 1 h at RT. After washing, the binding of the secondary was detected by adding the substrate 3,3′,5,5′-tetramethylbenzidine (TMB, BD Biosciences). The reaction was blocked with 0.5 M H_2SO_4 and the absorbance at 450 nm and reference 630 nm was measured.

Individual sera were titrated in parallel for the presence of VSV-specific IgG by end-point ELISA. Neutralizing dose 50 were measured as described (Sammicheli *et al*, 2016).

SARS-CoV-2 pseudovirus neutralization assay

SARS-CoV-2 pseudovirus neutralization assay was performed as previously described (Conforti *et al*, 2022). Briefly, lentiviral vector containing luciferase reporter were pseudotyped with B.1.1.529 SARS-CoV-2 spike protein and used for neutralization assay. HEK293T-hACE2 receptor were plated in 96-well plates and transduced with 0.05 MOI of SARS-CoV-2 pseudovirus that were subjected to 1 h at 37°C of preincubation with threefold serially diluted mice plasma. After 24 h of incubation, pseudoparticle cell transduction was measured by luciferase assay using Bright-Glo™ Luciferase System (Promega), and dose–response curves were generated by non-linear regression curve fitting to calculate Neutralization dose 50 (ND50).

Cell isolation and flow cytometry

Mice were euthanized by cervical dislocation. At the time of autopsy, mice were perfused through the right ventricle with PBS. Nasal turbinates were removed from the nose cavity. Lung tissue was digested in RPMI 1640 containing 3.2 mg/ml Collagenase IV (Sigma, #C5138) and 25 U/ml DNAse I (Sigma, #D4263) for 30 min at 37°C. Homogenized lungs were passed through 70 μm nylon meshes to obtain a single cell suspension. Cells were resuspended in 36% percoll solution (Sigma, #P4937) and centrifuged for 20 min at 653 *g* (light acceleration and low brake). The remaining red blood cells were removed with ACK lysis. Peripheral blood was collected in PBS 0.5 mM EDTA and lysed two times with ACK. Single-cell suspensions of spleens were generated as described (Sammicheli *et al*, 2016).

For analysis of *ex-vivo* intracellular cytokine production, 1 mg/ml of brefeldin A (Sigma, #B7651) was included in the digestion buffer. All flow cytometry stainings of surface-expressed and intracellular molecules were performed as described (Bénéchet *et al*, 2019; Fumagalli *et al*, 2021, 2022; Simone *et al*, 2021). Briefly, cells were stimulated for 4 h at 37°C in the presence of brefeldin A, monensin (life technologies, #00-4505-51), and a pool of overlapping peptides (1 μg/ml per peptide), including MHC class I- and MHC class II-restricted peptides (9–22 amino acids) covering the S, S1, S$^+$, M, and N protein of SARS-CoV-2 (Miltenyi, #130-126-700; #130-127-041; #130-127-311; #130-126-702, #130-126-698; Silva-Cayetano *et al*, 2021). In selected experiments (Appendix Fig S5), cells were stimulated with GP61 and GP33 peptides (2 μg/ml per peptide) (Iannacone *et al*, 2008). As positive control for IFN-γ and TNF-α production, cells were stimulated with PMA (Invitrogen, # 356150050) and Ionomycin (Invitrogen, #I24222). Cell viability was

---

The paper explained

Problem
Nirmatrelvir—an orally available inhibitor of the 3-chymotrypsin-like cysteine protease—has been shown to reduce the risk of progression to severe COVID-19. However, the impact of nirmatrelvir treatment on the development of SARS-CoV-2-specific adaptive immune responses is unknown.

Results
By using mouse models of SARS-CoV-2 infection, we show that nirmatrelvir administration blunts the development of SARS-CoV-2-specific antibody and T cell responses.

Impact
While the clinical data continue to support nirmatrelvir treatment for the prevention of severe COVID-19 in high-risk individuals, the data reported here draw attention to a potential negative impact of this therapy. We believe that our results might help explain the virological and/or symptomatic relapse after treatment completion reported in some individuals and should inform clinical and public health policies.

---

assessed by staining with Viobility™ 405/520 fixable dye (Miltenyi, Cat #130-109-814). In Fig 2H, biotinylated-RBD (26 KDa, kindly provided by L. Aurisicchio from Takis Biotech) were mixed with Alexa Fluor (AF)-647 or 488-fluorescent streptavidins (53 kDa) in a molar ratio of 4:1, respectively, to obtain fluorescent RBD tetramers at 2 µg/ml. RBD-specific B cells were labeled prior to the surface staining for 30 min at 4°C. Antibodies (Abs) are indicated in Appendix Table S2.

Flow cytometry analysis was performed on BD FACS Symphony A5 SORP, Cytek Aurora, and analyzed with FlowJo software (Treestar).

Confocal immunofluorescence histology

Mice were euthanized and perfused transcardially with PBS. One left lobe of the lung was collected and fixed in 4% paraformaldehyde for 16 h, then dehydrated in 30% sucrose prior to embedding in OCT freezing media (Killik Bio-Optica #05-9801). Twenty micrometer sections were cut on a CM1520 cryostat (Leica) and adhered to Superfrost Plus slides (Thermo Scientific). Sections were permeabilized and blocked in PBS containing 0.3% Triton X-100 (Sigma-Aldrich) and 0.5% BSA followed by staining in permeabilization buffer of Foxp3 / Transcription Factor Staining Buffer Set (eBioscence, # 00-5523-00). Slides were stained for Ki-67 (eBioscence, Clone SolA15, # 56-5698-82) and B220 (Biolegend, Clone RA3-6B2, #103228) overnight at RT. Lung sections were washed twice for 5 min and stained with DAPI (Life Technologies, #D1360) for 5 min at RT, then washed again, and mounted for imaging with FluorSaveTM Reagent (Merck Millipore, #345789). Images were acquired on an SP5 or SP8 confocal microscope with 20× objective (Leica Microsystem). To minimize fluorophore spectral spillover, the Leica sequential laser excitation and detection modality was used.

Statistical analyses and software

Detailed information concerning the statistical methods used is provided in the figure legends. Flow data were collected using FlowJo

Version 10.5.3 (Treestar). Statistical analyses were performed with GraphPad Prism software version 8 (GraphPad). Immunohistochemical imaging analyses were performed with QuPath (Quantitative Pathology & Bioimage 5 Analysis) software. *N* represents individual mice analyzed per experiment. Experiments were performed independently at least twice to control for experimental variation. Error bars indicate the standard error of the mean (SEM). In selected experiments (Fig 1B and C, Appendix Figs S1A and B, and S4D), error bars indicate the standard deviation (SD). Dose–response curves for IC_{50} values were determined by non-linear regression. We used Mann–Whitney *U*-tests to compare two groups with non-normally distributed continuous variables and Kruskal–Wallis non-parametric test or one-way ANOVA test to compare three or more unpaired groups. Normality of data distribution was tested with a Shapiro–Wilk normality test and normality was chosen only when normality could be confirmed for each dataset. We used two-way ANOVA followed by Sidak's multiple comparisons tests to analyze experiments with multiple groups and two independent variables. Significance is indicated as follows: $*P < 0.05$; $**P < 0.01$; $***P < 0.001$. Comparisons are not statistically significant unless indicated.

Data availability

All data are available in the main text or the appendix file. This study includes no data deposited in external repositories.

Expanded View for this article is available online.

Author contributions

Disclosure and competing interests statement

MI participates in advisory boards/consultancies for Gilead Sciences, Third Rock Ventures, Antios Therapeutics, Asher Bio, GentiBio, Clexio Biosciences, Sybilla, BlueJay Therapeutics. LGG is a member of the board of directors at Genenta Science and participates in advisory boards/consultancies for Antios Therapeutics, Chroma Medicine, Ananda Immunotherapies, and Gilead Sciences. RDF is a consultant for Moderna and a member of the board of directors of T-One Therapeutics.

For more information

i https://www.covid19treatmentguidelines.nih.gov/therapies/antivirals-including-antibody-products/ritonavir-boosted-nirmatrelvir--paxlovid-/
ii https://www.iannaconelab.com/
iii https://twitter.com/iannaconelab?lang=en

References

Badovinac VP, Porter BB, Harty JT (2004) CD8+ T cell contraction is controlled by early inflammation. *Nat Immunol* 5: 809−817

Bénéchet AP, Simone GD, Lucia PD, Cilenti F, Barbiera G, Bert NL, Fumagalli V, Lusito E, Moalli F, Bianchessi V *et al* (2019) Dynamics and genomic landscape of CD8+ T cells undergoing hepatic priming. *Nature* 574: 200−205

Boucau J, Uddin R, Marino C, Regan J, Flynn JP, Choudhary MC, Chen G, Stuckwisch AM, Mathews J, Liew MY *et al* (2022) Characterization of Virologic rebound following Nirmatrelvir-ritonavir treatment for coronavirus disease 2019 (COVID-19). *Clin Infect Dis* 76: e526−e529

Cannalire R, Cerchia C, Beccari AR, Leva FSD, Summa V (2022) Targeting SARS-CoV-2 proteases and polymerase for COVID-19 treatment: state of the art and future opportunities. *J Med Chem* 65: 2716−2746

Charness M, Gupta K, Stack G, Strymish J, Adams E, Lindy D, Mohri H, Ho D (2022a) Rapid relapse of symptomatic omicron SARS-CoV-2 infection following early suppression with Nirmatrelvir/ritonavir. *Research Square* https://doi.org/10.21203/rs.3.rs-1588371/v2 [PREPRINT]

Charness ME, Gupta K, Stack G, Strymish J, Adams E, Lindy DC, Mohri H, Ho DD (2022b) Rebound of SARS-CoV-2 infection after Nirmatrelvir−ritonavir treatment. *N Engl J Med* 387: 1045−1047

Conforti A, Marra E, Palombo F, Roscilli G, Ravà M, Fumagalli V, Muzi A, Maffei M, Luberto L, Lione L *et al* (2022) COVID-eVax, an electroporated DNA vaccine candidate encoding the SARS-CoV-2 RBD, elicits protective responses in animal models. *Mol Ther* 30: 311−326

Corbin GA, Harty JT (2004) Duration of infection and antigen display have minimal influence on the kinetics of the CD4+ T cell response to listeria monocytogenes infection. *J Immunol* 173: 5679−5687

Costanzi E, Kuzikov M, Esposito F, Albani S, Demitri N, Giabbai B, Camasta M, Tramontano E, Rossetti G, Zaliani A *et al* (2021) Structural and biochemical analysis of the dual inhibition of MG-132 against SARS-CoV-2 Main protease (Mpro/3CLpro) and human Cathepsin-L. *Int J Mol Sci* 22: 11779

Dai EY, Lee KA, Nathanson AB, Leonelli AT, Petros BA, Brock-Fisher T, Dobbins ST, MacInnis BL, Capone A, Littlehale N *et al* (2022) Viral kinetics of severe acute respiratory syndrome coronavirus 2 (SARS-CoV-2) omicron infection in mRNA-vaccinated individuals treated and not treated with Nirmatrelvir-Ritonavir. *medRxiv* https://doi.org/10.1101/2022.08.04.22278378 [PREPRINT]

Fu L, Ye F, Feng Y, Yu F, Wang Q, Wu Y, Zhao C, Sun H, Huang B, Niu P *et al* (2020) Both Boceprevir and GC376 efficaciously inhibit SARS-CoV-2 by targeting its main protease. *Nat Commun* 11: 4417

Fumagalli V, Ravà M, Marotta D, Lucia PD, Laura C, Sala E, Grillo M, Bono E, Giustini L, Perucchini C *et al* (2021) Administration of aerosolized SARS-CoV-2 to K18-hACE2 mice uncouples respiratory infection from fatal neuroinvasion. *Sci Immunol* 7: eabl9929

Fumagalli V, Venzin V, Lucia PD, Moalli F, Ficht X, Ambrosi G, Giustini L, Andreata F, Grillo M, Magini D *et al* (2022) Group 1 ILCs regulate T cell−mediated liver immunopathology by controlling local IL-2 availability. *Sci Immunol* 7: eabi6112

Giovanni MD, Cutillo V, Giladi A, Sala E, Maganuco CG, Medaglia C, Lucia PD, Bono E, Cristofani C, Consolo E *et al* (2020) Spatiotemporal regulation of type I interferon expression determines the antiviral polarization of CD4+ T cells. *Nat Immunol* 21: 321−330

Gupta K, Strymish J, Stack G, Charness M (2022) Rapid relapse of symptomatic SARS-CoV-2 infection following early suppression with Nirmatrelvir/ritonavir.

Halfmann PJ, Iida S, Iwatsuki-Horimoto K, Maemura T, Kiso M, Scheaffer SM, Darling TL, Joshi A, Loeber S, Singh G *et al* (2022) SARS-CoV-2 omicron virus causes attenuated disease in mice and hamsters. *Nature* 603: 687−692

Hammond J, Leister-Tebbe H, Gardner A, Abreu P, Bao W, Wisemandle W, Baniecki M, Hendrick VM, Damle B, Simón-Campos A *et al* (2022) Oral Nirmatrelvir for high-risk, nonhospitalized adults with Covid-19. *N Engl J Med* 386: 1397−1408

Iannacone M, Sitia G, Isogawa M, Whitmire JK, Marchese P, Chisari FV, Ruggeri ZM, Guidotti LG (2008) Platelets prevent IFN-α/β-induced lethal hemorrhage promoting CTL-dependent clearance of lymphocytic choriomeningitis virus. *Proc Natl Acad Sci U S A* 105: 629−634

Jin Z, Du X, Xu Y, Deng Y, Liu M, Zhao Y, Zhang B, Li X, Zhang L, Peng C *et al* (2020) Structure of Mpro from SARS-CoV-2 and discovery of its inhibitors. *Nature* 582: 289−293

Kuzikov M, Costanzi E, Reinshagen J, Esposito F, Vangeel L, Wolf M, Ellinger B, Claussen C, Geisslinger G, Corona A *et al* (2021) Identification of inhibitors of SARS-CoV-2 3CL-pro enzymatic activity using a small molecule in vitro repurposing screen. *Acs Pharmacol Transl Sci* 4: 1096−1110

Luan X, Chen B, Shang W, Yin W, Jin Y, Zhang L, Xu HE, Zhang S (2022) Structure basis for inhibition of SARS-CoV-2 by the feline drug GC376. *Acta Pharmacol Sin* 44: 255–257

Ma C, Sacco MD, Hurst B, Townsend JA, Hu Y, Szeto T, Zhang X, Tarbet B, Marty MT, Chen Y *et al* (2020) Boceprevir, GC-376, and calpain inhibitors II, XII inhibit SARS-CoV-2 viral replication by targeting the viral main protease. *Cell Res* 30: 678–692

Mercado R, Vijh S, Allen SE, Kerksiek K, Pilip IM, Pamer EG (2000) Early programming of T cell populations responding to bacterial infection. *J Immunol* 165: 6833–6839

Najjar-Debbiny R, Gronich N, Weber G, Khoury J, Amar M, Stein N, Goldstein LH, Saliba W (2022) Effectiveness of Paxlovid in reducing severe COVID-19 and mortality in high risk patients. *Clin Infect Dis* 76: e342–e349

Owen DR, Allerton CMN, Anderson AS, Aschenbrenner L, Avery M, Berritt S, Boras B, Cardin RD, Carlo A, Coffman KJ *et al* (2021) An oral SARS-CoV-2 Mpro inhibitor clinical candidate for the treatment of COVID-19. *Science* 374: 1586–1593

Pillaiyar T, Manickam M, Namasivayam V, Hayashi Y, Jung S-H (2016) An overview of severe acute respiratory syndrome–coronavirus (SARS-CoV) 3CL protease inhibitors: Peptidomimetics and small molecule chemotherapy. *J Med Chem* 59: 6595–6628

Ramirez SI, Grifoni A, Weiskopf D, Parikh UM, Heaps A, Faraji F, Sieg SF, Ritz J, Moser C, Eron JJ *et al* (2022) Bamlanivimab therapy for acute COVID-19 does not blunt SARS-CoV-2-specific memory T cell responses. *JCI Insight* 7: e163471

Ranganath N, O'Horo JC, Challener DW, Tulledge-Scheitel SM, Pike ML, O'Brien RM, Razonable RR, Shah A (2022) Rebound phenomenon after Nirmatrelvir/ritonavir treatment of coronavirus Disease-2019 in high-risk persons. *Clin Infect Dis* 76: e537–e539

Sammicheli S, Kuka M, Lucia PD, de Oya NJ, Giovanni MD, Fioravanti J, Cristofani C, Maganuco CG, Fallet B, Ganzer L *et al* (2016) Inflammatory monocytes hinder antiviral B cell responses. *Sci Immunol* 1: eaah6789

Shuai H, Chan JF-W, Hu B, Chai Y, Yuen TT-T, Yin F, Huang X, Yoon C, Hu J-C, Liu H *et al* (2022) Attenuated replication and pathogenicity of SARS-CoV-2 B.1.1.529 omicron. *Nature* 603: 693–699

Silva-Cayetano A, Foster WS, Innocentin S, Belij-Rammerstorfer S, Spencer AJ, Burton OT, Fra-Bidó S, Lee JL, Thakur N, Conceicao C *et al* (2021) A booster dose enhances immunogenicity of the COVID-19 vaccine candidate ChAdOx1 nCoV-19 in aged mice. *Med (N Y)* 2: 243–262

Simone GD, Andreata F, Bleriot C, Fumagalli V, Laura C, Garcia-Manteiga JM, Lucia PD, Gilotto S, Ficht X, Ponti FFD *et al* (2021) Identification of a Kupffer cell subset capable of reverting the T cell dysfunction induced by hepatocellular priming. *Immunity* 54: 2089–2100

Soares H, Baniecki ML, Cardin R, Leister-Tebbe H, Zhu Y, Guan S, Hyde C, He W, Wang Z, Hao L *et al* (2022) Viral load rebound in placebo and Nirmatrelvir-ritonavir treated COVID-19 patients is not associated with recurrence of severe disease or mutations. *N Engl J Med* 387: 1047–1049

V'kovski P, Kratzel A, Steiner S, Stalder H, Thiel V (2021) Coronavirus biology and replication: implications for SARS-CoV-2. *Nat Rev Microbiol* 19: 155–170

Wang L, Berger NA, Davis PB, Kaelber DC, Volkow ND, Xu R (2022a) COVID-19 rebound after Paxlovid and Molnupiravir during January–June 2022. *medRxiv* https://doi.org/10.1101/2022.06.21.22276724 [PREPRINT]

Wang L, Volkow ND, Davis PB, Berger NA, Kaelber DC, Xu R (2022b) COVID-19 rebound after Paxlovid treatment during omicron BA.5 vs BA.2.12.1 subvariant predominance period. *medRxiv* https://doi.org/10.1101/2022.08.04.22278450 [PREPRINT]

Wong L-YR, Zheng J, Wilhelmsen K, Li K, Ortiz ME, Schnicker NJ, Thurman A, Pezzulo AA, Szachowicz PJ, Li P *et al* (2022) Eicosanoid signaling blockade protects middle-aged mice from severe COVID-19. *Nature* 605: 146–151